ELSEVIER

Polymer 43 (2002) 3279–3293

polymer

www.elsevier.com/locate/polymer

Influence of β nucleation on the mechanical properties of isotactic polypropylene and rubber modified isotactic polypropylene

C. Grein[a,1], C.J.G. Plummer[a,*], H.-H. Kausch[a], Y. Germain[b], Ph. Béguelin[a]

[a]*Laboratoire de Polymères, Département des Matériaux, Ecole Polytechnique Fédérale de Lausanne (EPFL), Lausanne CH-1015, Switzerland*
[b]*AtoFina, Feluy, B-7181, Belgium*

Received 22 October 2001; received in revised form 6 February 2002; accepted 8 February 2002

Abstract

The tensile and fracture behaviour of neat α and β nucleated isotactic polypropylene and rubber-modified α and β nucleated isotactic polypropylene has been investigated at test speeds of 0.0001–10 ms^{-1} in the temperature range −30 to +60 °C. The presence of the β phase had little effect at low temperature. However, at +25 and +60 °C, it increased the speeds corresponding to the ductile–brittle transition in the neat polymer by more than three decades. This behaviour has been linked to changes in microdeformation mechanisms observed at the lamellar and spherulitic level, an increase in cavitational deformation in tensile tests and an increase in the strength of the β relaxation in dynamic mechanical spectra. In the blends, the presence of the β phase led to somewhat higher energy dissipation in regimes of ductile fracture. However, the ductile–brittle transitions were not significantly affected. The modifier phase was therefore inferred to control the initiation and propagation of the plastic zone ahead of the crack tip during fracture.

Keywords: Polypropylene; Toughening; β phase

1. Introduction

Improving the fracture resistance of rubber toughened materials requires control of both the matrix and the modifier properties. The effects of the modifier content and its morphology in isotactic polypropylene (iPP) toughened with ethylene propylene diene monomer (EPDM) or ethylene propylene rubber (EPR) core-shell particles have been widely studied [1–13]. That of matrix polymorphism has received far less attention, however, although it has been known since the early 1960s that iPP can crystallize in at least three different forms (α, β and γ) [14–16].

Under standard synthesis and processing conditions, the relatively stable monoclinic α-modification is the dominant phase. It is typically characterized by auto-epitaxial growth of lenticular lamellae, elongated in the [100] direction, giving rise to the so-called 'cross-hatched' morphology in which two distinct populations of lamellae are arranged with their long axes roughly perpendicular locally [17,18]. The hexagonal β phase lamellae are relatively broad and form coplanar stacks whose plane tends to twist about the growth direction, often giving rise to spherulites with banded textures when observed between crossed polarizers [15,18]. Although β spherulites appear only sporadically in mouldings of commercial grades of iPP, their proportion can be increased by using certain mineral or organic nucleating agents [19–21].

β nucleated iPP homopolymers are of particular interest in that they have been reported to show improved impact resistance, the increase in fracture energy ranging from 25 to 300% depending on the molar mass, the β phase content, the temperature, the test speed and the test procedure [22–29]. This suggests that β nucleation might also enhance the impact resistance of iPP/EPR for a given modifier content, providing the motivation for the present work, in which its influence has been investigated systematically using a variety of techniques. To avoid the dynamic effects characteristic of conventional impact testing (Charpy and Izod tests), the impact resistance has been assessed using quasi-static high speed tensile testing [30,31]. Since the same apparatus may be used for conventional static testing, this approach has the additional advantage of allowing direct comparison of results obtained over a wide range of test speeds.

* Corresponding author. Tel.: +41-21-693-2856; fax: +41-21-693-5868.
E-mail address: christopher.plummer@epfl.ch (C.J.G. Plummer).
[1] Present address: Borealis GmbH, St-Peter-Straße 25, A-4021 Linz, Austria.

0032-3861/02/$ - see front matter
PII: S0032-3861(02)00135-0

Table 1
Physico-chemical characteristics of the materials investigated

	Rubber content[a] (%)	Mean particle diameter[b] (nm)	Matrix crystalline structure	Matrix M_n (g/mol)	Matrix M_w (g/mol)	Degree of crystallinity (%)
α-0	0	–	α	47,880	248,100	34.7 ± 0.5
β-0	0	–	α (20%) + β (80%)	46,440	237,000	35 ± 4
α-15/420	15	428	α	44,370	231,600	34.9 ± 0.7
β-15/420	15	414	α (35%) + β (65%)	43,540	232,800	35 ± 4

[a] Nominal modifier contents, subsequently verified by image analysis of TEM micrographs.
[b] From image analysis of TEM micrographs (mean values for 1000–2000 particle sections).

2. Experimental

2.1. Materials and basic characterization

Four materials were studied: an α iPP homopolymer (α-0), a β nucleated iPP homopolymer (β-0), an α iPP/EPR blend (α-15/420) and a β nucleated iPP/EPR blend (β-15/420). The blends contained 15 vol% EPR and the β-nucleating agent was from Borealis. All the materials were supplied as $100 \times 100 \times 4\ mm^3$ injection moulded plaques and dog-bone-shaped tensile test specimens with $10 \times 4\ mm^2$ rectangular cross-sections. M_w and M_n (Table 1) were determined by gel permeation chromatography (GPC).

The melting point and degree of crystallinity of the α phase (Table 1) were measured by differential scanning calorimetry (DSC) at $10\ K\ min^{-1}$ on 5–10 mg samples, taking the enthalpy of fusion of 100% crystalline α iPP to be $207\ J\ mol^{-1}$ [32]. As shown in Fig. 1, four different melting peaks were observed in DSC heating scans, depending on the material. The peak at 166 °C is characteristic of the α phase and the peak at 125 °C in the blends is attributed to CH_2-rich regions of the EPR particles (see Section 2.2). The origin of the two peaks at 141 and 150 °C observed in the β-modified materials (marked β_1 and β_2 in Fig. 1), and typical of relatively low crystallisation temperatures, is thought to be melting and re-crystallisation during the scan [33]. The β phase and α phase contents could not therefore be quantified by DSC in a straightforward manner in this case.

Wide angle X-ray scattering (WAXS; Siemens Kristalloflex 805 diffractometer) provided an alternative means of determining the degree of crystallinity and the β phase content of the β nucleated specimens. Fig. 2 shows results for the different materials. The overall degree of crystallinity, determined from the sum of the crystalline peak intensities divided by the total scattered intensity, was 35 ± 4% in each case, consistent with the DSC data for the α phase. The β phase content of the matrix was estimated from

$$K_x = \frac{H(300)}{H(300) + H_\alpha},$$

where $H(300)$ is the height of the β 300 peak at $2\theta = 16.2°$ and H_α is the sum of the heights of the α peaks [16]. It is also possible to derive an order parameter S for the β phase from

$$S = \frac{H(300)}{H(300) + H(301)},$$

where $H(301)$ is the height of β 301 peak at $2\theta = 21°$. Results for the specimen cores are shown in Table 1. Consistent with previous observations [22,34], the β phase content was somewhat reduced in a 150–200 μm thick skin layer at the specimen surface, present in all the materials (about 51 and 27.5% in β-0 and β-15/420, respectively). The EPR particles were also apparently detrimental to β

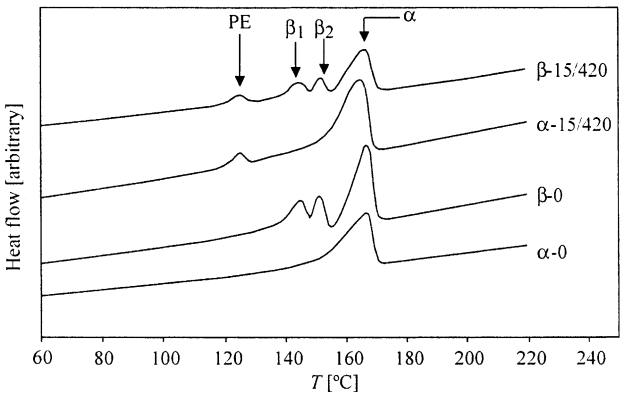

Fig. 1. DSC heating scans at 10 K/min.

nucleation, although the β phase remained the majority phase in the cores of specimens of the β nucleated blend.

Dynamic mechanical analysis (DMA) was performed on $52 \times 12 \times 3\ mm^3$ rectangular specimens taken from the centre of the 4 mm thick plaques, using a Rheometrics RSA II. Fig. 3 shows DMA temperature scans (10 K/min at 1 Hz). The β relaxation of the matrix, generally associated with T_g [35,36], was at 5 °C in α-0 and α-15/420; β nucleation resulted in an increase of about 2 K in the peak temperature of this relaxation as well as a significant increase in its strength. The rubber modified materials showed another strong relaxation at about −55 °C associated with the T_g of the EPR. Two further relaxations were also present; the α_c relaxation at 60 °C, attributed to diffusion of crystallographic defects in the iPP matrix lamellae [37], and the γ relaxation at 60 °C in α-0 and 70 °C in β-0, which is a secondary relaxation of the amorphous regions of the matrix [36].

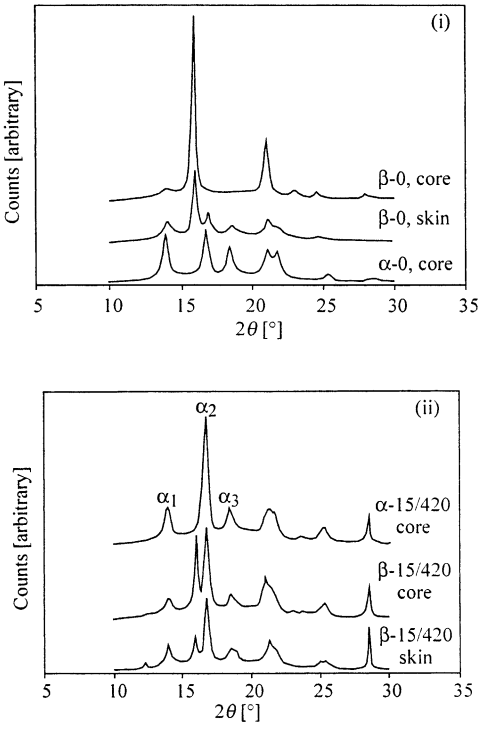

Fig. 2. WAXS data for (i) α-0 and β-0, and (ii) α-15/420 and β-15/420, taken from the skin and the core regions of injection moulded specimens.

2.2. Morphological characterization

Thin sections (140 nm) were prepared for transmission electron microscopy (Philips CM20 TEM operating at 200 kV) at room temperature from surfaces stained in 5 wt% aqueous RuO_4 for about 24 h, using a Reichert Jung Ultracut-E ultramicrotome and a 45° diamond knife. As shown in Fig. 4, scanning electronic microscopy (Philips XLF30 FEG-SEM operating at 4–6 kV) of gold-coated RuO_4 stained surfaces in back-scattered mode (SEM/BSE) [38–41] also provided detailed morphological information. Moreover, SEM/BSE is particularly convenient for the observation of relatively large areas of the specimen, often required in fractography, for example, and involves simpler sample preparation than TEM. Both techniques indicated the blends to have similar modifier particle size distributions and dispersions, the diameters of particle sections ranging from about 50 to 3 μm with a mean of about 420 nm (Table 1). The smaller particle sections showed a core-shell structure, whereas the larger particles contained multiple cores; the shells consisted of amorphous EPR penetrated by matrix lamellae emanating from the matrix particle interface, and the cores contained CH_2-rich lamellar inclusions.

2.3. Fracture testing

Mode I fracture mechanics tests made use of compact tension (CT) specimens, tested with a Schenk high-speed servo-hydraulic tensile test apparatus at 0.0001–10 ms^{-1}. At speeds greater than 0.1 ms^{-1}, a damping pad was placed on the pick-up unit to reduce transient acceleration of the specimens, so that quasi-static stress conditions could be assumed [30,31], permitting static fracture mechanics analysis of the data [42]. In what follows, linear elastic fracture mechanics (LEFM) has been applied throughout. Although the conditions for strictly valid LEFM testing were not met over the full range of temperatures and test speeds, this allowed consistent analysis of all the data. The apparent critical stress intensity factors, K_{Imax}, were calculated from

$$K_{Imax} = f(a/W)\frac{F_{max}}{B\sqrt{W}}$$

where a is the length of the pre-crack, B is the specimen thickness, W is the specimen width (here $a/W = 0.5$), $f(a/W)$ is a dimensionless geometrical factor and F_{max} is force maximum [43]. The apparent critical strain energy release rate for crack initiation, G_{Imax}, was determined from U_{ini}, the area under the force–displacement curves

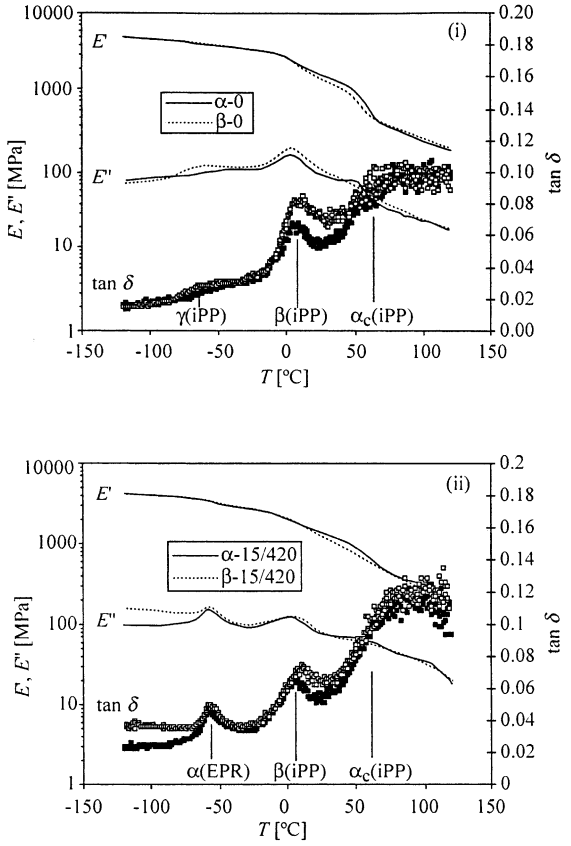

Fig. 3. DMA data for (i) α-0 and β-0, and (ii) α-15/420 and β-15/420.

up to F_{max}, using

$$G_{Imax} = \frac{U_{ini}}{BW\Phi(a/W)}$$

where $\Phi(a/W)$ is a dimensionless geometrical factor [43]. The test rate was expressed in terms of the crack tip loading rate, dK/dt, given by

$$dK/dt = f(a/W)\frac{dF/dt}{B\sqrt{W}},$$

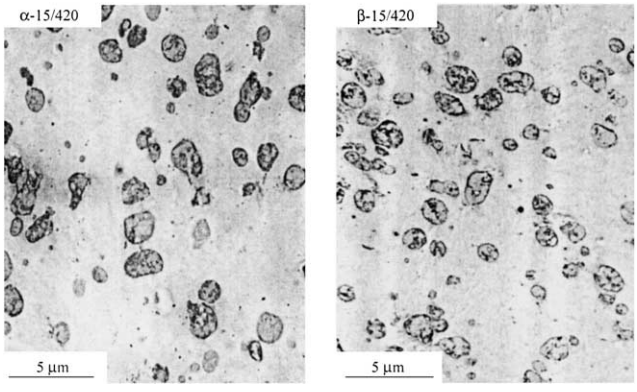

Fig. 4. Morphology of α-15/420 and β-15/420 (SEM/BSE of RuO_4 stained specimens).

which accounts implicitly for variations in specimen stiffness (arising from variations in a and the rate dependence of the modulus).

To observe sub-critical microdeformation at the crack tip it was necessary to arrest crack propagation. At low speeds, the specimens could be unloaded manually, but at high speeds, crack arrest was achieved by testing two nominally identical specimens in series, failure of one specimen instantaneously unloading the other prior to complete failure [30]. The damage zone was maintained in tension by inserting a wedge between the crack faces and specimens immersed for about 24 h in 5 wt% aqueous RuO_4, so that the stain was able to penetrate the damage zone via the crack tip. After trimming, an internal surface perpendicular to the crack plane was exposed and the morphology observed by either SEM/BSE or TEM.

2.4. Tensile testing

A series of tensile tests was carried out in order to obtain further insight into the deformation mechanisms, although it should be borne in mind that the non-equivalence of local strain rates in simple tension and CT tests at any given test speed makes quantitative extrapolation to these latter difficult. The tensile tests were performed on the dog-bone specimens at 25 °C and at 0.0001–1 ms^{-1} (approximately equivalent to strain rates of 0.001–10 s^{-1}). To separate contributions from different mechanisms to the overall tensile strain, ε, the sample volume was monitored using simultaneous longitudinal and lateral extensometry. Following Frank and Lehmann [44], the elastic strain, ε_{elast}, was calculated assuming a constant elastic modulus, E, derived from the tangent of the stress–strain curve as $\varepsilon \rightarrow 0$. The permanent cavitational strain, ε_{cav}, was calculated from

$$\varepsilon_{cav} = (1+\varepsilon)(1+\varepsilon_{lat})^2 - 1 - \varepsilon_{elast}(1-2\nu_{elast})$$

where $\varepsilon_{elast} = \sigma/E$ is the elastic strain, ε is the total strain, ε_{lat} is the lateral strain and ν_{elast} is the instantaneous Poisson's ratio. The shear strain, ε_{shear}, was taken to be

$$\varepsilon_{shear} = \varepsilon - \varepsilon_{elast} - \varepsilon_{cav}.$$

3. Results

3.1. Fracture behaviour of the neat α and β nucleated specimens

Typical force–displacement curves for the neat polymers are given in Fig. 5 for $T > T_g$ and in Fig. 6 for $T < T_g$. These were considered to reflect either brittle or ductile behaviour, depending on whether there was discontinuous drop in force at or close to the force maximum. For $T > T_g$ the fracture behaviour was sensitive to the crystalline structure; whereas β-0 was ductile up to 200 MPa $m^{1/2}$ s^{-1} (0.1 ms^{-1}) at 25 °C and up to 800 MPa $m^{1/2}$ s^{-1} (0.4 ms^{-1}) at 60 °C, α-0 was relatively brittle over nearly the whole range of test speeds

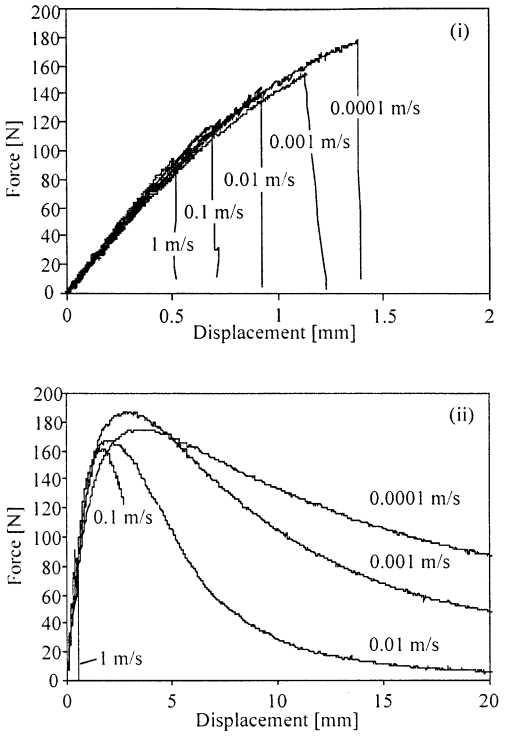

Fig. 5. Typical force–displacement curves for CT fracture specimens at 25 °C: (i) α-0 and (ii) β-0.

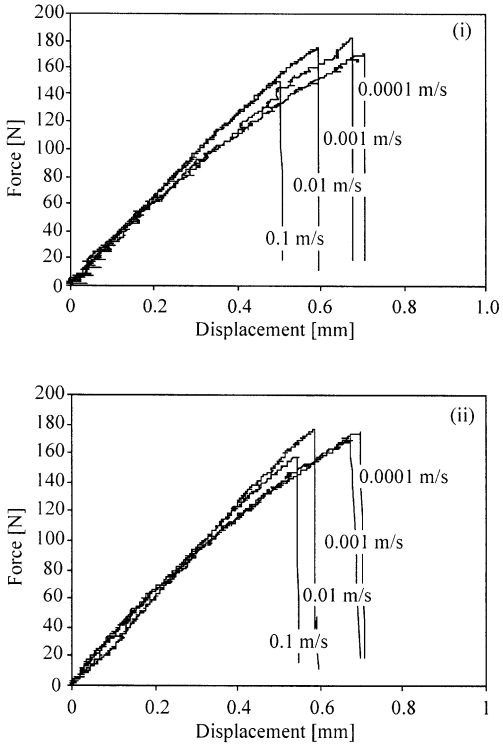

Fig. 6. Typical force–displacement curves for CT fracture specimens at −5 °C: (i) α-0 and (ii) β-0.

and temperatures (the exception being 0.0001 ms^{-1} at 60 °C). Thus, at 25 °C, β nucleation resulted in an increase in the test speed corresponding to the ductile–brittle transition by more than three decades. To put this into perspective, only one decade of speed separates the ductile–brittle transition of iPP/15 vol% EPR from that of iPP/30 vol% EPR with similar matrix M_n and M_w to those of the materials studied here and containing predominantly α spherulites [3]. The brittle behaviour of α-0 was attributed to the inability of the crack tip damage zone to propagate, since the slight non-linearity in the force–displacement curves suggested some damage accumulation prior to crack initiation at low test speeds. The stabilising effect of the β phase on crack propagation up to test speeds close to 0.1 ms^{-1} was remarkable in comparison. However, for $T < T_g$, both α-0 and β-0 showed brittle behaviour.

K_{Imax} is shown as a function of dK/dt in Fig. 7 for temperatures between −30 and 60 °C. In each case, K_{Imax} remained roughly constant up to about 200 MPa $m^{1/2}$ s^{-1} but decreased strongly at higher rates. It was nevertheless consistently higher in β-0 than in α-0 at 25 and 60 °C and at test rates in the vicinity of the β-0 ductile–brittle transition (indicated by the arrows in Fig. 7). The positive contribution of β nucleation to the fracture resistance of iPP at $T > T_g$ was also reflected by G_{Imax} as shown in Fig. 8. Although it had little influence below T_g, the presence of the β phase resulted in a substantial increase in G_{Imax} at 25° for low and intermediate test rates. At 60 °C, G_{Imax} was greater in β-0 than in α-0 up to the highest test speeds, although it converged to a value of about 30 kJ m^{-2} at 0.0001 ms^{-1} in both cases, reflecting the onset of ductile fracture in α-0.

Specimens of α-0 tested at 0.0001 ms^{-1} and 25 °C showed a rough fracture surface, characteristic of cracking and crazing along multiple planes and residual stress whitening at the notch tip confirmed there to have been a certain amount of damage accumulation prior to initiation. However, there was no stress whitening associated with crack propagation. Moreover, at the highest test speeds (1 ms^{-1} or more), the fracture surface became mirror-like at the notch tip, and stress whitening was suppressed, suggesting initiation and breakdown of a single craze ahead of the crack tip, as has been observed previously in α-iPP under similar conditions [13].

In β-0 deformed in the ductile fracture regime, stress whitening was not only observed at the notch tip, but also at the tips of propagating cracks. The internal structure of the stress whitened zone at the tip of crack in a sample tested at 0.001 ms^{-1} and 25 °C, and which had been arrested after a certain amount of propagation, is shown in Figs. 9 and 10. It consisted principally of a dense bundle of nearly parallel crazes, which merged to form a continuous fibrillar structure adjacent to the crack faces. As shown in Fig. 9(ii), there was a correlation between the craze loci and the spherulitic structure. Crazes apparently initiated either along the spherulite equators, i.e. the diameters perpendicular to the loading direction, or in the corresponding polar regions, where the lamellae were roughly parallel to the loading direction,

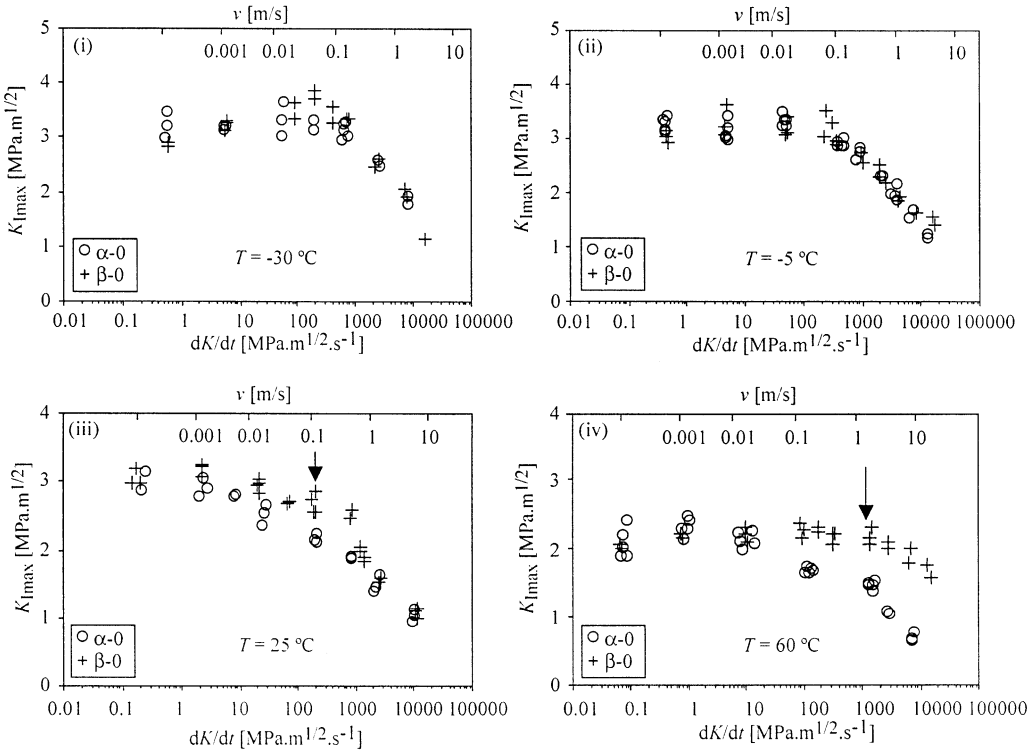

Fig. 7. K_{Imax} vs. dK/dt at (i) −30 °C, (ii) −5 °C, (iii) 25 °C and (iv) 60 °C for α-0 and β-0. The upper scale gives an indication of the test speed. The arrows indicate the ductile–brittle transitions in β-0.

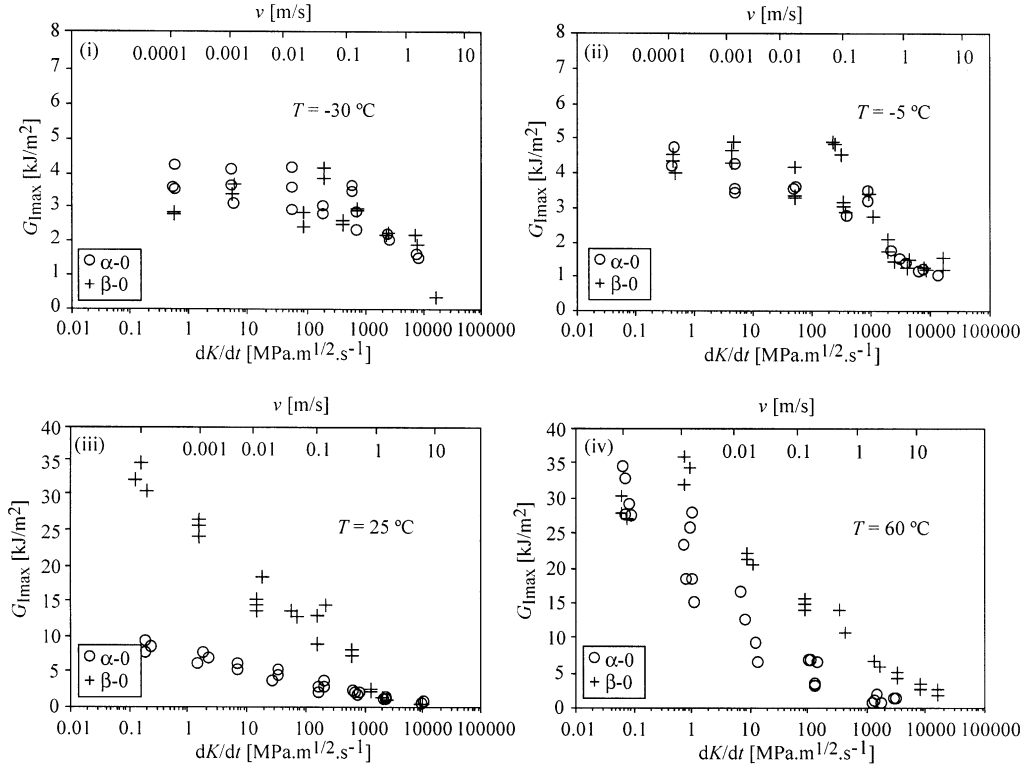

Fig. 8. G_{Imax} vs. dK/dt at (i) −30 °C, (ii) −5 °C, (iii) 25 °C and (iv) 60 °C for α-0 and β-0. The upper scale gives an indication of the test speed.

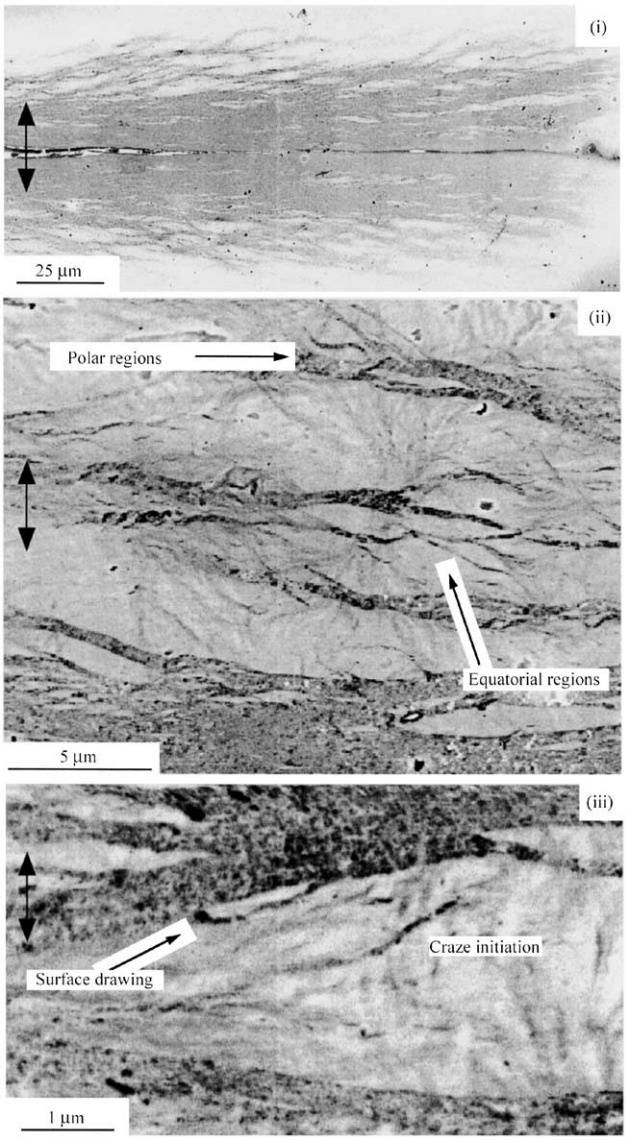

Fig. 9. SEM/BSE images of microdeformation in β-0 tested at 0.001 ms^{-1} and 25 °C: (i) overview of the crack tip damage zone; (ii) and (iii) details from the periphery of the damage zone. The arrows indicate the direction of the applied load.

consistent with previous observations [27,45–48]. The early stages of crazing, shown in detail in Figs. 9(iii) and 10, involved interlamellar separation and cavitation where the lamellae were at high angles to the loading direction, resulting in diffuse deformation zones in which individual relatively undeformed lamellae were visible (Fig. 10(b)). The subsequent shear deformation of these lamellae then led to the formation of a fibrillar deformation zone or craze (Fig. 10(c), cf. the Peterlin model [49]). Where the lamellae were at low angles to the loading direction, the interface between the undeformed material and the crazes was relatively well defined (Fig. 10(d)); only occasional isolated cavities were visible beyond the main crazes in such regions, consistent with recent AFM observations [48]. However, in regions of intermediate lamellar orientation, not only diffuse regions of interlamellar cavitation, but also regions of pronounced shear banding were often present in the early stages of deformation, the shear bands being reflected by abrupt discontinuities in the lamellar trajectories.

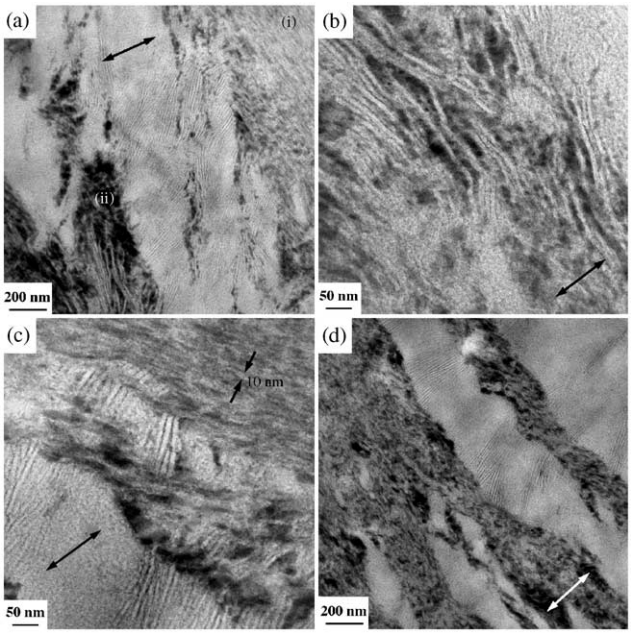

Fig. 10. TEM images of microdeformation in β-0 tested at 0.001 ms^{-1} and 25 °C: (a) overview of diffuse interlamellar separation and cavitation and part of a fibrillar deformation zone or craze (top right-hand side of the image); (b) detail of the early stages of craze formation in a region in which the direction of the applied load was roughly perpendicular to the lamellar trajectories; (c) detail of the edge of a fibrillar deformation zone (top right-hand side of the image) showing partly relaxed fibrillar structure; (d) overview of fibrillar deformation zones in a region in which the direction of the applied load was roughly parallel to the lamellar trajectories, again showing partly relaxed fibrillar structure. The arrows indicate the direction of the applied load.

The damage zone corresponding to high speed brittle fracture in β-0 was also somewhat different to that observed in α-iPP under comparable conditions. As shown in Fig. 11 for a specimen tested at 1 ms^{-1} and 25 °C, there was far less extensive damage than in β-0 tested at lower speeds, but multiple crazing and a certain amount of crack bifurcation remained visible along the flanks and at the tips of arrested cracks. The trajectories of these features were again apparently correlated with the spherulitic texture.

3.2. Fracture behaviour of the α and β nucleated iPP/EPR blends

The evolution of the force–displacement curves with test speed was similar in CT specimens of α-15/420 and β-15/420, as shown in Figs. 12 and 13, for example. A ductile–brittle transition with increasing test rate was observed in each case, moving to higher test rates as the temperature was increased. As shown in Fig. 14, the blends also showed similar K_{Imax} over the whole range of temperature and test

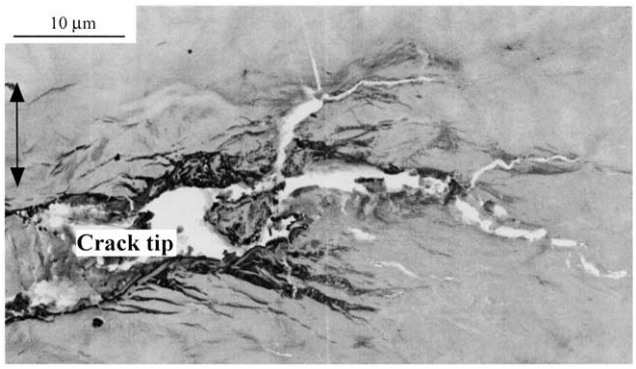

Fig. 11. SEM/BSE images of microdeformation in β-0 tested at 1 ms^{-1} and 25 °C. The arrows indicate the direction of the applied load.

speed investigated. At 5 °C and above, K_{Imax} increased linearly with the logarithm of the test rate up to the ductile–brittle transition, which corresponded to the position of maximum in K_{Imax} vs. dK/dt, indicated by the arrows in Fig. 14. This increase was assumed to reflect a logarithmic dependence of the yield stress on strain rate deduced from tensile tests (see Section 3.3). The sharp drop in K_{Imax} beyond the transition corresponded to a marked decrease in the size of a stress whitened zone visible at the notch tip with increasing test rate and hence to a progressive suppression of the damage mechanisms responsible for toughening at low speeds. These trends were again reflected by G_{Imax} (Fig. 15). As in the neat polymers, β nucleation led to an increase in G_{Imax} at a given deformation rate for $T > T_g$, which was most marked at 25 °C. However, as shown in Fig. 16, unlike in the neat polymers, there was little change in the ductile–brittle transition speed.

There was correspondingly little difference in the microdeformation mechanisms in α-15/420 and β-15/420. Representative micrographs from crack tips in CT specimens tested at 0.001 ms^{-1} and 25 °C are shown in Fig. 17. Cavitation within the particles and in the interphase between the particles and the matrix was prevalent in the early stages of damage, but closer to the crack tip, matrix crazing became highly developed. The global orientation of the craze trajectories appeared to be normal to the direction of the average principal stress. However, locally, the origins and trajectories of the crazes were strongly correlated with the (cavitated) modifier particles; crazes initiated at the modifier particles and their tips tended to be deflected towards neighbouring modifier particles. Consequently, the cavitated particles and crazes formed a continuous network close to the crack tip and plane strain conditions could no longer be considered effective, regardless of the global stress-state. Substantial shear flow as well as crazing was therefore assumed to have preceded ultimate failure, giving rise to the central wedge-shaped region of the crack-tip damage zone; considerable distortion of the matrix ligaments is

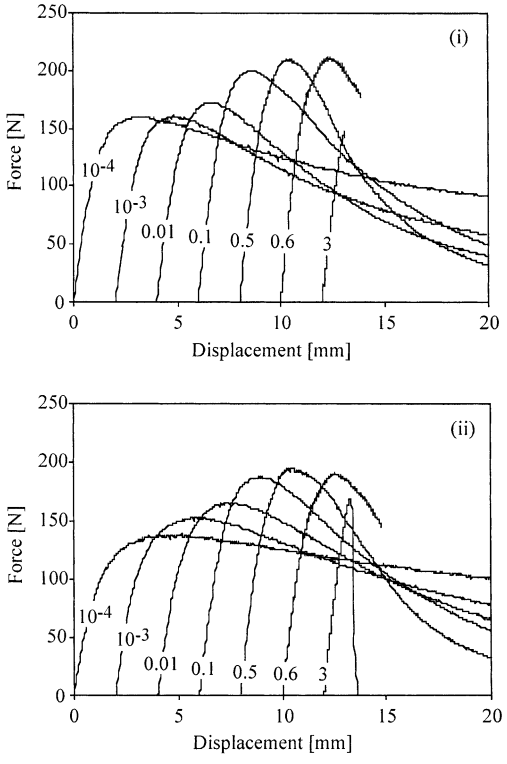

Fig. 12. Typical force–displacement curves for CT fracture specimens at $T = 25$ °C : (i) α-15/420 and (ii) β-15/420. The speed indicated on each curve is in ms^{-1}.

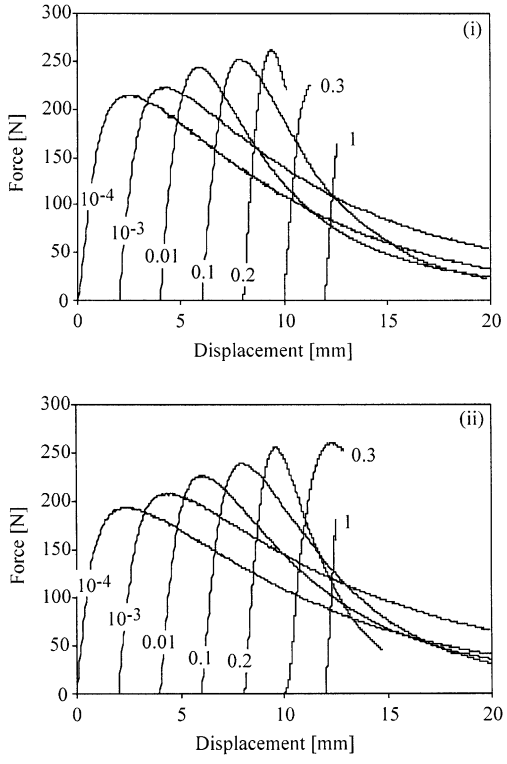

Fig. 13. Typical force–displacement curves for CT fracture specimens at $T = -5$ °C : (i) α-15/420 and (ii) β-15/420. The speed indicated on each curve is in ms^{-1}.

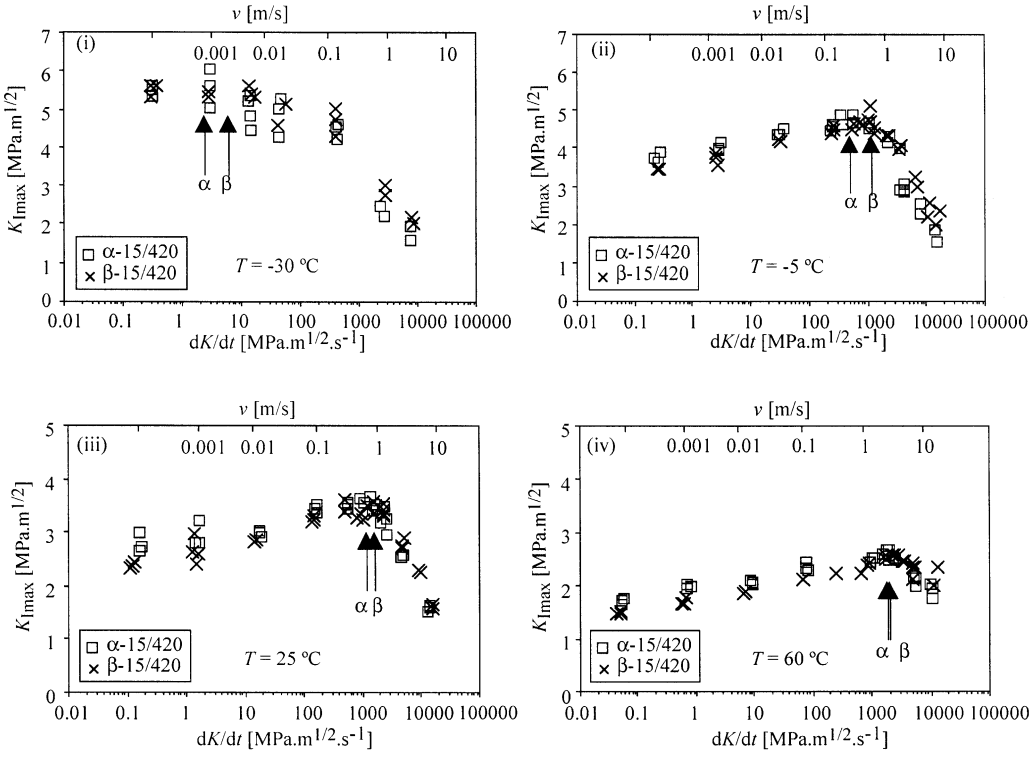

Fig. 14. K_{Imax} vs. dK/dt at (i) −30 °C, (ii) −5 °C, (iii) 25 °C and (iv) 60 °C for α-15/420 and β-15/420. The upper scale gives an indication of the test speed. The arrows indicate the ductile–brittle transitions.

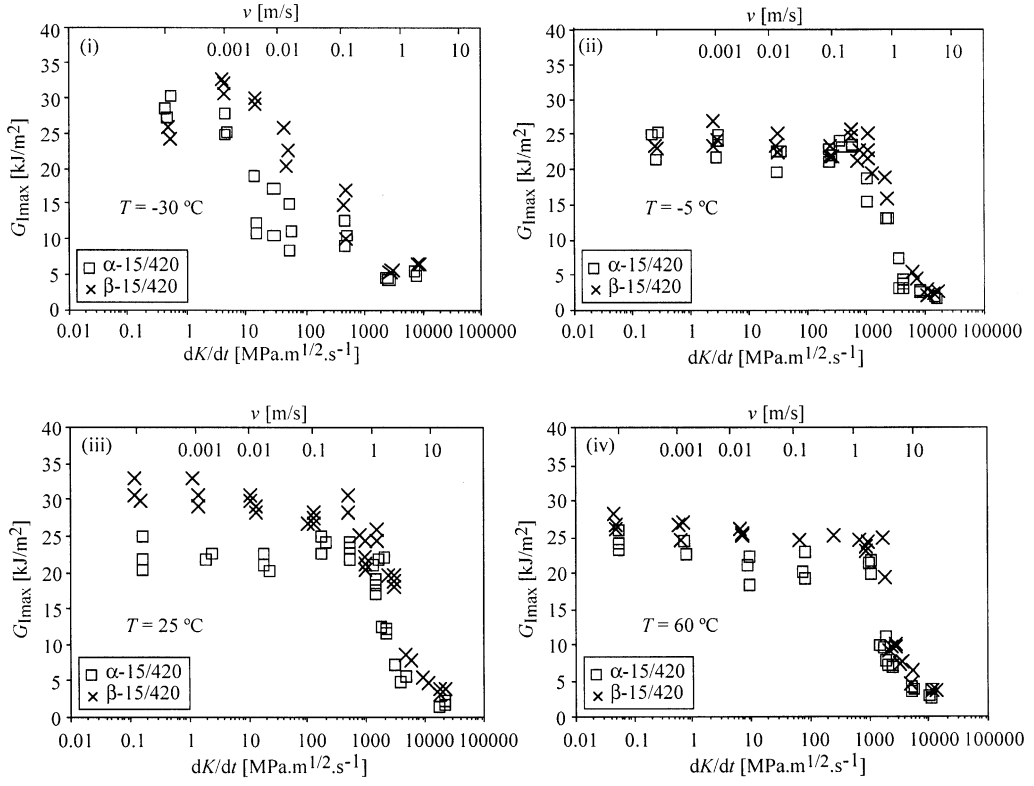

Fig. 15. G_{Imax} vs. dK/dt at (i) −30 °C, (ii) −5 °C, (iii) 25 °C and (iv) 60 °C for α-15/420 and β-15/420. The upper scale gives an indication of the test speed.

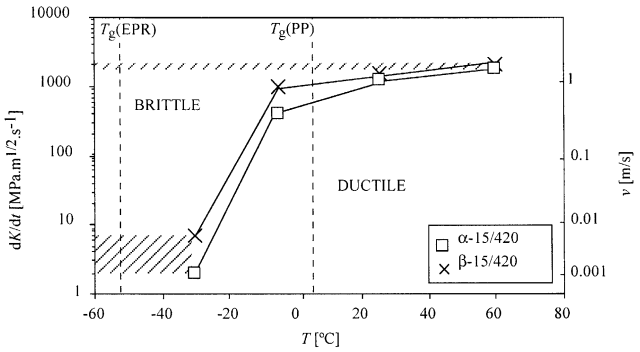

Fig. 16. Ductile–brittle transition rates vs. temperature for α-15/420 and β-15/420. The right-hand scale gives an indication of the test speed. The T_gs of the EPR and the matrix are also indicated on the temperature axis.

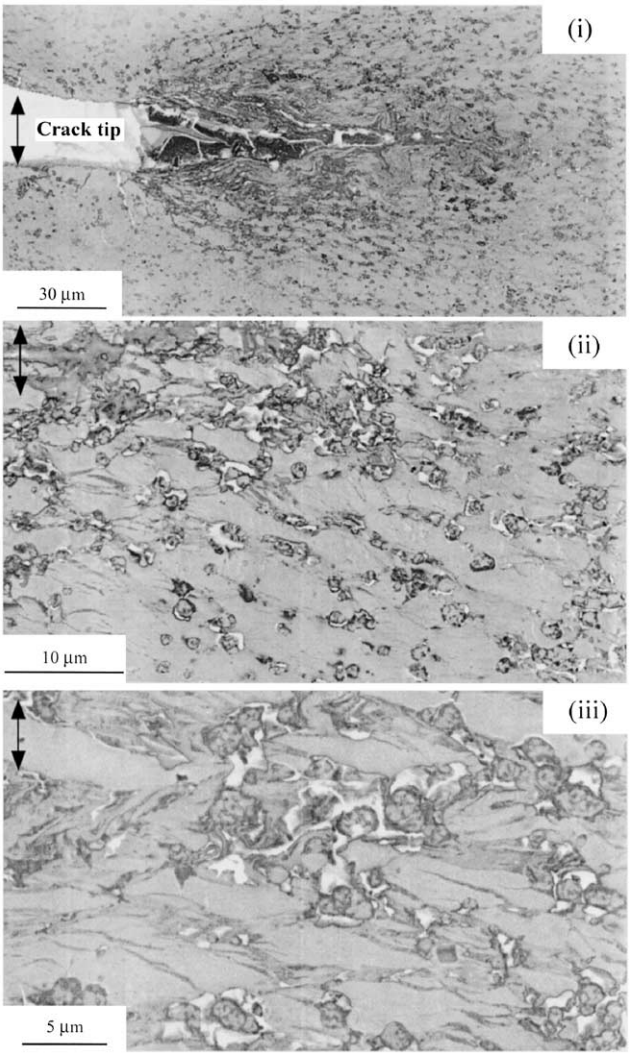

Fig. 17. SEM/BSE images of microdeformation in α-15/420 and β-15/420 tested at 0.001 ms^{-1} and 25 °C: (i) overview of the crack tip in α-15/420; (ii) detail of the deformation gradient in α-15/420 (increased deformation on moving from the lower right-hand corner to the top left-hand corner of the image); (iii) detail of microdeformation in β-15/420. The arrows indicate the direction of the applied load.

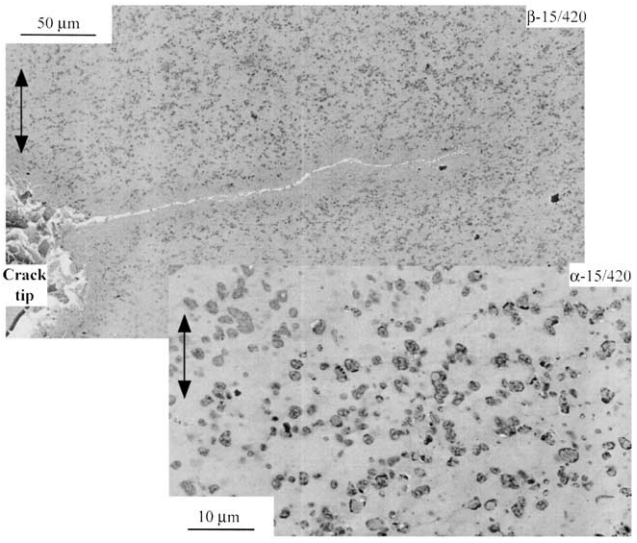

Fig. 18. SEM/BSE images of microdeformation in α-15/420 and β-15/420 tested at 3 ms^{-1} and 25 °C. The arrows indicate the direction of the applied load.

visible adjacent to the crack faces and at the crack tip in Fig. 17.

Fig. 18 shows the microdeformation behaviour in a specimen tested at 3 ms^{-1}, where brittle behaviour was observed. Ahead of the notch tip, a single crack was visible in both α-15/420 and β-15/420. As shown in the higher magnification image in Fig. 18, cavitated particles were visible at the periphery of the crack, but crazing was very limited in extent in each case.

3.3. Simple tensile deformation

The yield stress, σ_y, taken to correspond to the maximum in the nominal stress–strain curves obtained from simple tensile tests, was significantly lower in the β nucleated materials than in their unmodified counterparts over a wide range of temperatures and strain rates, as shown in Fig. 19. Fig. 20 gives a break-down of the different contributions to the overall strain, ε, as a function of this latter in β-0 at 25 °C, derived from the stress–strain curves as described in Section 2. Qualitatively similar trends were observed in all the materials, and may be summarized as follows:

- ε_{elast} was substantially independent of the test speed;
- the cavitational strain onset preceded yield, as observed previously in other systems [50,51]; the non-linearity in the force displacement curves prior to yield or, in the case of the CT tests, prior to the force maximum, could not therefore be attributed to iso-volumetric flow alone;
- the cavitational strain onset depended on the strain rate; the higher the test speed, the lower the value of ε at which cavitation was first observed; in β-0 at 25 °C and 10 s^{-1} the onset was at $\varepsilon \approx 2\%$ and at 0.001 s^{-1} it was at

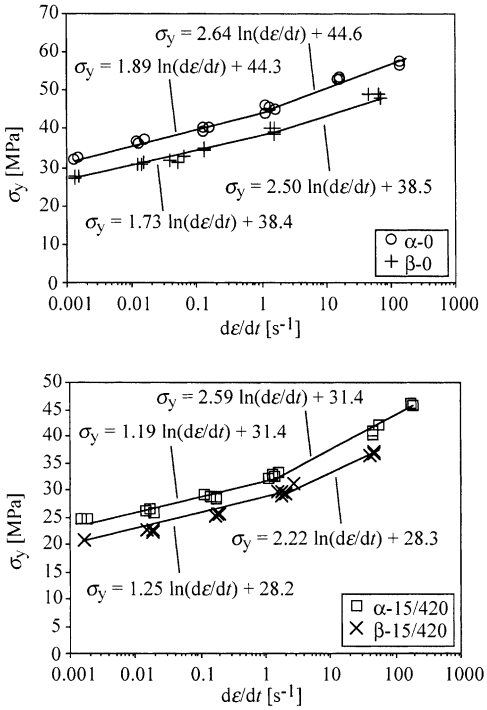

Fig. 19. Yield stress as a function of strain-rate at different temperatures for the different materials.

$\varepsilon \approx 7\%$; similar observations have been reported for polyoxymethylene [51], suggesting that above a certain strain rate dependent threshold, iso-volumetric interlamellar deformation can no longer accommodate the global deformation;

- for a given ε, $\varepsilon_{cav}/\varepsilon$ increased markedly with strain rate, ranging from 5% at 0.001 s^{-1} to 38% at 10 s^{-1} at $\varepsilon = 0.1$ in β-0 at 25 °C, for example, again consistent with observations in other systems [50,52]; between 0.001 and 1 s^{-1}, the extent of cavitation at any given ε increased almost linearly with the logarithm of the strain rate, possibly indicating it to be a thermally activated process.

Fig. 21 illustrates this last point further, showing $\varepsilon_{cav}/\varepsilon$ for $\varepsilon = 0.15$ and different strain rates in α-0 and β-0 at 25 °C. In both materials, cavitational processes dominated at the highest strain rates. Nevertheless, even at low rates, ε_{cav} was significantly greater in β-0 than in α-0 under equivalent conditions.

Data are given for α-15/420 and β-15/420 in Fig. 22. In this case, ε_{cav} (assumed to include particle cavitation and matrix cavitation) did not change significantly with the nature of the matrix, consistent with a dominant role of the rubber particles in damage development. Moreover, ε_{cav} in the blends was substantially higher than in the neat polymers at a given ε.

4. Discussion

A number of possible explanations have been evoked in the past to explain the differences in mechanical behaviour of the α and β phases, and these will now briefly be reconsidered in the light of the present results.

A mechanically induced β to α phase transformation has often been referred to in discussions of the relative ductility of β nucleated materials [23,25,53–55]. That the phase transformation took place in the present case was confirmed

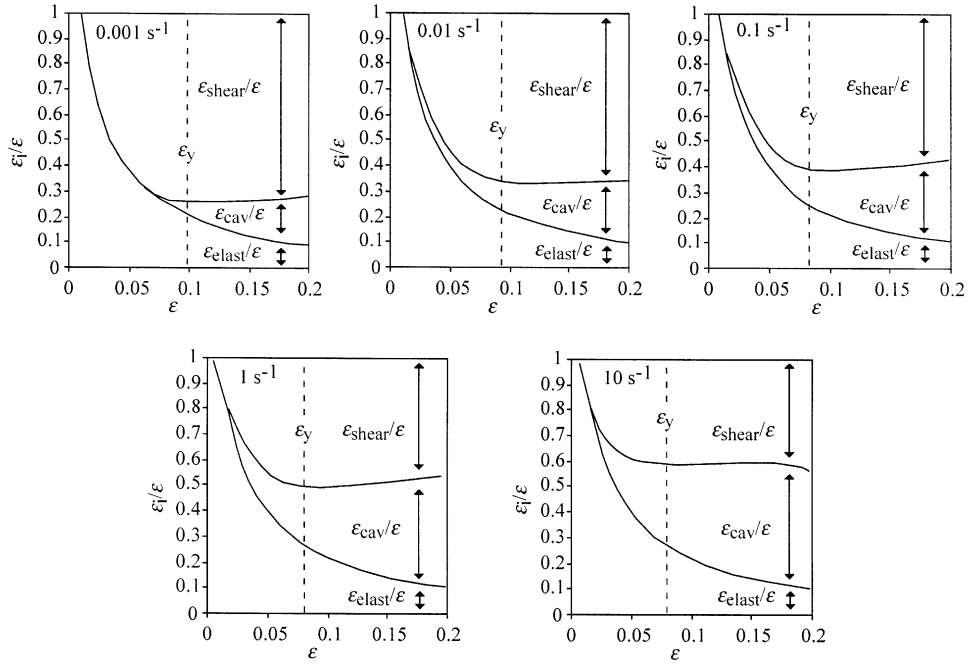

Fig. 20. $\varepsilon_{elast}/\varepsilon$, $\varepsilon_{cav}/\varepsilon$ and $\varepsilon_{shear}/\varepsilon$ vs. ε for β-0 tested at between 0.001 and 10 s^{-1} at 25 °C.

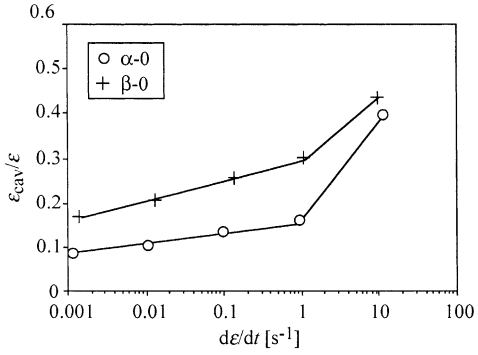

Fig. 21. $\varepsilon_{cav}/\varepsilon$ vs. dε/dt at $\varepsilon = 0.15$ and 25 °C for α-0 and β-0.

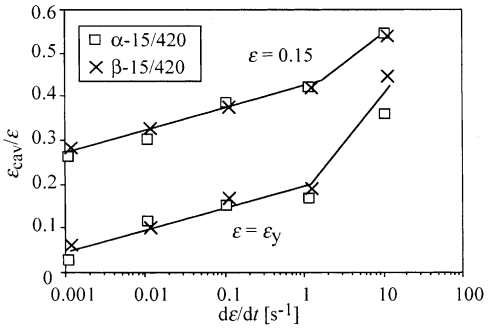

Fig. 22. $\varepsilon_{cav}/\varepsilon$ vs. dε/dt at $\varepsilon = 0.15$ and 25 °C for α-15/420 and β-15/420.

by WAXS, as shown in Table 2, which gives results for dog-bone specimens tested at 0.0001 ms^{-1}, and in Table 3, which gives results from fracture surfaces in CT specimens tested at between 0.0001 and 0.1 ms^{-1}. The tensile tests indicated the β to α phase transition to depend strongly on the extent of deformation, its being considerably less advanced in un-necked whitened regions of the samples than in the main ductile neck. The order parameter associated with the β phase also decreased with the extent of deformation in the tensile specimens. In the post-mortem fracture surfaces of the CT specimens, the transformation was apparently less pronounced than in the tensile tests, particularly at the highest test speeds. Indeed, similar measurements on impact tested β iPP have been taken to imply the β to α phase transformation to be suppressed [29]. However, the extent of the damage zones is usually limited in CT specimens, making it difficult to draw general conclusions from such results.

Since the density of the β phase (0.921 g cm^{-3}) is lower than that of the α phase (0.936 g cm^{-3}), it has been suggested that a β to α phase transition during bulk deformation may promote cavitation [53]. The results in Section 3.3 confirmed the β phase to favour the development of microcavities in deformed iPP, as widely reported elsewhere [22,27,29,53,56,57]. However, this need not imply a causal relationship between the onset of cavitation and the deformation-induced β to α phase transformation. Moreover, a stress-induced volume decrease in the crystalline regions of the sample is unlikely to have been at the origin of the interlamellar cavitation in Fig. 10, say, given that the lamellae were relatively undeformed at this stage. (Electron diffraction has shown the transition to be associated with micronecking in thin films [58], which would be consistent with the observation by X-ray that it is essentially associated with macroscopic necking in the bulk samples.)

Spherulite size is another important factor in the fracture behaviour of iPP, large spherulites often promoting brittleness owing to the concentration of structural defects and impurities at their boundaries, and hence easy crack propagation paths over relatively long distances [22,56,59]. Labour [27] has varied the spherulite diameter in β-iPP using thermal treatments designed to ensure that other structural parameters, such as the lamellar thickness, remain constant. He observed a threefold increase in the room temperature critical strain energy release rate for crack propagation on reducing the spherulite diameter from 50–10 μm. In the present case, the spherulite diameters in the core of the β-0 specimens were about 10 μm, whereas

Table 2
β phase content and order parameter, S, in different parts of tensile specimens of β nucleated materials tested at 0.0001 ms^{-1} and 25 °C

	Undeformed		Whitened zone		Neck	
	β content (%)	S	β content (%)	S	β content (%)	S
β-0	80	76	62.5	75.3	37.5	61.5
β-15/420	66.5	72	61.5	61.9	36.8	57

Table 3
β phase content and order parameter, S, at the fracture surface of CT specimens of β nucleated materials tested at between 0.0001 and 0.1 ms^{-1} at 25 °C

	0.0001 ms^{-1}		0.001 ms^{-1}		0.01 ms^{-1}		0.1 ms^{-1}	
	β content (%)	S	β content (%)	S	β content (%)	S	β content (%)	S
β-0	70	70	79	72	79	73.5	76	70
β-15/420	44	64	51.5	62	64.5	66.5	65	68.5

they were about 50 μm in the α-0 specimens. In both α-15/420 and β-15/420, on the other hand, the spherulite diameters were about 5 μm. On this basis, therefore, the differences in the spherulitic size alone could account for the relatively brittle behaviour of α-0, although there was no direct evidence for this. (For example, there was no preferential failure at the spherulite boundaries in any of the specimens investigated here.)

Morphological explanations have also been advanced for the reduced σ_y of the β nucleated materials. These generally focus on the lamellar morphology rather than the spherulite size, the interlocked cross-hatched morphology of the α structure being argued to hinder certain slip mechanisms [45,60]. This is supported by recent work on the compression of bulk alpha PP [61]; crystallographic slip on (010)[001] and (100)[001] is activated in the early stages of deformation, although (010)[001] has a lower critical resolved shear stress. Thus σ_y is expected to be higher than if this latter slip system were activated immediately. In the later stages of yielding, where the initial morphology is less critical, it is the (010)[001] system that dominates, implying a large yield drop, consistent with results from tensile tests, and hence a strong tendency for slip processes to localize (possibly favouring localized crazing in tension).

In α iPP, crazes are indeed more localized and better defined than in β iPP (for a given molecular weight). For example, the trajectories of crazes observed on the iPP side of relatively weak reaction bonded α iPP/polyamide-6 interfaces subject to mode I opening follow the plane of the interfaces. Isolated β iPP spherulites, on the other hand, provoke significant deviation of crazes and/or crack tips from the interface and nucleation of secondary crazes beyond the interface (in the equatorial or polar regions of the β spherulites) [62]. The results presented in Section 3.1 for β-0, as well as results from past microdeformation studies [47], also indicate tensile deformation of the bulk β phase to result in relatively delocalized, inhomogeneous modes of deformation (mixed shear and crazing). Since the observed textures are strongly correlated with the local orientation of the β lamellae with respect to the tensile axis, the trend towards more localized deformation in α spherulites may also reflect the more uniform lamellar textures of these latter.

The low toughness at high speeds at 25 °C in both β and α iPP and the strong strain rate dependence of $\varepsilon_{cav}/\varepsilon$ are thought to be due to the proximity of the range of temperatures corresponding to the β relaxation in the dynamic measurements. Under these conditions, there may be insufficient mobility for homogeneous deformation in the amorphous regions to keep pace with the highest deformation rates, leading to brittle behaviour similar to that observed at lower temperatures. At 60 °C, where the β relaxation is fully activated, its relatively high strength in the β phase may continue to contribute to the fracture resistance at high rates, although α processes will also play an increased role as the temperature is raised [36].

More generally, regardless of the specific nature of the relevant relaxation processes and their influence on the fracture mechanisms, the higher molecular mobility associated with the β phase above T_g will be expected to (i) reduce the quantity of elastic energy stored at a given strain, delaying the onset of instabilities and (ii) promote energy dissipation during crack propagation [22,29,63–65]. (The differences in σ_y referred to earlier can also be explained, at least in part, by the relatively high intrinsic molecular mobility of the β phase as reflected by changes in the strength and position of its relaxation peaks [36].) Care should nevertheless be taken in too detailed an interpretation of the results from high speed fracture testing in these terms, since the local strain rates are not well defined and since heat evolution may become significant at high speeds, particularly in the more ductile samples; a 90 K rise in temperature has been reported for toughened iPP at speeds of $10\,ms^{-1}$, for example Ref. [10].

Any or all of the aforementioned factors may play a significant role in the observed behaviour and it is difficult to discriminate between them directly on the basis of the present results. Moreover, although some aspects of these results may be considered to demonstrate improved fracture resistance in β iPP, it is difficult to attach a precise significance to K_{Imax} and G_{Imax} when the criteria for LEFM are not strictly satisfied. For example, given that the effect of β nucleation on the modulus was relatively minor, certain observations of large differences in G_{Imax} in specimens with similar K_{Imax} could not be directly reconciled with LEFM. However, these differences in G_{Imax} were correlated with improved crack propagation resistance in the β nucleated samples, as reflected by the large shifts in the ductile–brittle transition speed in the neat polymers. Similar trends were also observed in the total energy to fracture, i.e. the total area under the force–displacement curves in the CT tests. Such quantities are likely to be geometry dependent, but the overall trends were consistent with reported improvements in the Charpy or Izod fracture toughness of iPP on β nucleation, demonstrating the usefulness of the ductile–brittle transition as a complement to fracture mechanics parameters nominally associated with crack initiation.

In the modified blends, sub-critical cavitation was dominated by cavitation associated with the rubber particles. It follows that the initiation of matrix deformation during both crack initiation and propagation, and the extent of damage delocalization (e.g. multiple crazing), were insensitive to the morphology of the matrix, consistent with the insensitivity of K_{Imax} to β nucleation. Below the matrix T_g, it is not surprising that β nucleation made little difference to the behaviour of the blends, given the similar response of the neat α and β nucleated specimens in this regime. The small increases in G_{Imax} in the β nucleated specimens above the matrix T_g may have reflected improved matrix ductility, but activation of crazing and shear deformation was sufficient to ensure ductile fracture up to relatively high test speeds in

both the α and β nucleated blends. It is perhaps significant that above the matrix T_g, the ductile–brittle transitions occurred at about the same test speeds in the blends as in the neat β nucleated specimens, suggesting the extent of high speed toughening to be matrix limited; if the matrix deformation is unable to develop, crack propagation will be brittle regardless of the effect of the modifier on the initiation of matrix deformation. This implies the differences in the fracture behaviour of the neat α and β nucleated specimens to be primarily morphological in origin. The similar behaviour observed below the matrix T_g nevertheless indicates that in order for specific features of the spherulitic or lamellar morphology to contribute to toughening, the amorphous phase must be sufficiently mobile, underlining the important role of the β relaxation. Rubber toughening, on the other hand, is limited by the T_g of the modifier and may still be effective below the matrix T_g.

5. Conclusions

The enhanced ductility of iPP containing a β phase nucleant resulted in an increase in the speed corresponding to its brittle–ductile transition in CT tests by at least three decades at $T > T_g$. This behaviour was correlated with extensive microcavitation in the form of a dense zone of craze-like structures at the crack tips, and cavitation was shown by volume extensometry in simple tensile tests to be more extensive in β nucleated specimens than in specimens containing predominantly α spherulites. However, at $T < T_g$, no significant differences in behaviour were observed, both neat α and β nucleated specimens showing relatively brittle behaviour down to the lowest test speeds investigated.

In rubber modified iPP, β nucleation had little effect on the brittle–ductile transition at any temperature and for T less than the matrix T_g, the ductile–brittle transitions occurred at comparable test speeds to those in the neat β nucleated specimens. This provides an indication of the important role of the rubber particles in initiating matrix deformation during crack initiation and propagation. The morphology and the mobility of the amorphous phase were therefore inferred to be crucial to the improved performance of the neat β nucleated specimens.

Acknowledgements

The authors are grateful to AtoFina for sponsoring this work, to the Electron Microscopy Centre (CIME) of the EPFL for their technical support and to Sandrine Grospellier for her contribution to the experimental work.

References

[1] Chou CJ, Vijayan K, Kirby D, Hiltner A, Baer E. J Mater Sci 1988;23:2533.
[2] Fernando PI, Williams JG. Polym Engng Sci 1983;21:1003.
[3] Grein C, Béguelin P, Plummer CJG, Kausch H-H, Tézé L, Germain Y. In: Williams JG, Pavan A, editors. Fracture of polymers, composites and adhesives, ESIS publications 27. Oxford: Elsevier, 2000. p. 319.
[4] Hodgkinson JM, Savadori A, Williams JG. J Mater Sci 1983;18:2319.
[5] Jang BZ, Uhlmann DR, Van der Sanden JB. Polym Engng Sci 1985;25:98.
[6] Jang BZ, Uhlmann DR, Van der Sanden JB. J Appl Polym Sci 1985;30:2485.
[7] Starke JU, Michler GH, Grellmann W, Seidler S, Gahleitner M, Fiebig J, Nezbedova E. Polymer 1998;39:75.
[8] Tjong SC, Li WD, Li KY. Polym Bull 1997;38:721.
[9] Van der Waal A, Nijhof R, Gaymans RJ. Polymer 1999;40:6031.
[10] Van der Waal A, Gaymans RJ. Polymer 1999;40:6045.
[11] Van der Waal A, Verheul AJJ, Gaymans RJ. Polymer 1999;40:6067.
[12] Liang JZ, Li RKY. J Appl Polym Sci 2000;77:409.
[13] Gensler R, Plummer CJG, Grein C, Kausch H-H. Polymer 2000;31:3809.
[14] Natta G, Corradini P. Suppl vol XV Ser X, Nuovo Cimento 1960;1:40.
[15] Keith HD, Padden FJJ, Walter NM, Wickhoff HW. J Appl Phys 1959;30:1485.
[16] Turner-Jones A, Aizlewood JM, Beckett DR. Makromol Chem 1964;75:134.
[17] Olley RH, Bassett DC. Polymer 1989;30:399.
[18] Norton DR, Keller A. Polymer 1985;26:704.
[19] Garbarczyk J, Paukzta D. Polymer 1981;22:562.
[20] Huang M-R, Li X-G, Fang B-O. J Appl Polym Sci 1995;56:1323.
[21] Varga JE. In: Karger-Kocsis J, et al., editors. Polypropylene: an A–Z reference. Dordrecht: Kluwer, 1999. p. 51.
[22] Karger-Kocsis J, Varga J, Ehrenstein GW. J Appl Polym Sci 1997;64:2057.
[23] Karger-Kocsis J. Polym Bull 1996;36:117.
[24] Karger-Kocsis J, Mouzakis DE, Ehrenstein GW, Varga J. J Appl Polym Sci 1999;73:1205.
[25] Karger-Kocsis J, Varga J. J Appl Polym Sci 1996;62:291.
[26] Gahleitner MW. J Appl Polym Sci 1996;61:649.
[27] Labour T. PhD Thesis. Ecole Centrale de Lyon, 1999.
[28] Tjong SC, Shen JS, Li RKY. Scripta Metallur Mater 1995;33:503.
[29] Tjong SC, Shen JS, Li RKY. Polymer 1996;37:2309.
[30] Béguelin P, Kausch H-H. In: Williams JG, Pavan A, editors. Impact and dynamic fracture of polymers and composites. London: Mechanical Engineering Publications, 1995.
[31] Béguelin P, Barbezat M, Kausch H-H. J Phys III France 1991;1:1867.
[32] Cheng SZD, Janimak JJ, Rodrigez J. In: Karger-Kocsis J, editor. Polypropylene: structure, blends and composites. London: Chapman & Hall, 1995.
[33] Vleeshouwers S. Polymer 1997;38:3213.
[34] Aboulfaraj M, Ulrich B, Dahoun A, G'Sell C. Polymer 1993;34:4817.
[35] Boyd RH. Polymer 1985;26:323.
[36] Jacoby P, Bersted BH, Kissel WJ, Smith CE. J Polym Sci 1986;24:461.
[37] Renecker DH, Mazur J. Polymer 1983;24:1387.
[38] Brown GM, Butler JH. Polymer 1997;38:1997.
[39] Goizueta G, Chiba T, Inoue T. Polymer 1992;33:886.
[40] Goizueta G, Chiba T, Inoue T. Polymer 1993;34:253.
[41] Vezie DL, Thomas EL, Adams WW. Polymer 1995;36:1761.
[42] Béguelin P, Fond C, Kausch H-H. Int J Fract 1998;89:85.
[43] Williams JG. European Structural Integrity Society, Test protocol TC4, 1990.
[44] Frank O, Lehmann J. Colloid Polym Sci 1986;264:473.
[45] Aboulfaraj M, G'Sell C, Ulrich B, Dahoun A. Polymer 1995;36:731.
[46] Li JX, Cheung WL, Chan CM. Polymer 1999;40:3641.
[47] Li JX, Cheung WL, Chan CM. Polymer 1999;40:2089.
[48] Voitot T. PhD Thesis. Université des Sciences et Technologies de Lille, 2000.
[49] Peterlin A. Polym Engng Sci 1977;17:183.

[50] Castagnet S, Gacougnolle J-L, Dang P. Mater Sci Engng 2000;A276:152.
[51] Scarramuzzino P. PhD Thesis. EPF Lausanne, 1998.
[52] Naqui SI, Robinson IM. J Mater Sci 1995;30:2446.
[53] Chu F, Yamaoka T, Ide H, Kimura Y. Polymer 1994;35:3442.
[54] Riekel C, Karger-Kocsis J. Polymer 1999;40:541.
[55] Li JX, Cheung WL. Polymer 1998;39:6935.
[56] Tjong SC, Shen JS, Li RKY. Polym Engng Sci 1996;36:100.
[57] Chu F, Yamaoka T, Kimura Y. Polymer 1995;36:2523.
[58] Plummer CJG, Kausch H-H. Macromol Chem Phys 1996;197:2047.
[59] Sandt A. Kunststoffe 1982;72:791.
[60] Coulon G, Castelein G, G'Sell C. Polymer 1999;40:95.
[61] Pluta M, Bartczak Z, Galeski A. Polymer 2000;41:2271.
[62] Plummer CJG, Kausch H-H, Creton C, Kalb F, Léger L. Proceedings of the European Conference on Macromolecular Physics EPS 98. Merseburg, Germany, 27 Sept–1 Oct, 1998.
[63] Ramsteiner F. Kunststoffe 1983;72:148.
[64] Karger-Kocsis J, Kulesnev VN. Polymer 1982;23:699.
[65] Vincent PI. Polymer 1974;15:111.